Journal of Applied Fluid Mechanics, Vol. 18, No. 3, pp. 821-834, 2025.
Available online at www.jafmonline.net, ISSN 1735-3572, EISSN 1735-3645.
https://doi.org/10.47176/jafm.18.3.2558

Numerical Research of the Water Entry of Hyperelastic Spheres Within Low Froude Numbers

L. Zhang, R. Xie and H. Jia†

National-Provincial Joint Engineering Laboratory for Fluid Transmission System Technology, Zhejiang Sci-Tech University, Hangzhou 310018, China

†*Corresponding Author Email: huixia.jia@zstu.edu.cn*

ABSTRACT

The water-entry process of solid and hollow hyperelastic spheres was numerically simulated using the arbitrary Lagrange–Euler method, based on the finite element analysis software LS-DYNA. The effect of the different initial velocities on the cavity evolution and deformation of the sphere in a range of low Froude (*Fr*) numbers was investigated. The evolution of the cavity, deformation of the hyperelastic sphere and parameters at the time of cavity closure were analysed. In addition, the difference in the water-entry process between solid and hollow spheres was given. The numerical results shows that the size of the cavity, fluctuation on the cavity profile, closure time and closure depth increased with *Fr* and that the closure time was proportional to $Fr^{1/2}$ for both solid and hollow spheres. However, the relationship between the closure depth and *Fr* of the hollow sphere differed from that of the solid one. Within the investigated low Froude numbers, whether for the solid or hollow spheres, the deformation amplitude increased with the Froude number. However, the deformation period remained nearly the same for different conditions. Under the same physical and motion parameters, the hollow sphere exhibited larger deformations compared with the solid sphere. The deformation period for the hollow sphere was also longer than that for the solid one.

Article History

Received January 1, 2024
Revised September 1, 2024
Accepted September 26, 2024
Available online January 1, 2025

Keywords:

Water entry
Fluid-structure interaction
Deformation
Cavity
Closure time

1. INTRODUCTION

The problem of water entry is prevalent in both nature and engineering applications, such as hunting behaviours of aquatic birds (Ropert-Coudert et al., 2004; Machovsky-Capuska et al., 2012), water-walking ability of amphibious lizards, water entry of a ship's bows (Xu et al., 1999), emergency water landing of aircraft (Kross et al., 1983) and water landing of re-entry capsules (Vaughan & United States, 1959; Thompson et al., 1965).

The water-entry process of an object comprises two phases: the first phase is the initial impact when an object that is initially in the air and moving downwards initiates contact with the water surface, and in the second stage, cavities (in most cases) form and develop around the object during the downwards movement of the object. At the initial stage of impact, an extremely large impact load is generated when the object bumps with the free surface, which may cause damage to biological organisms or mechanical components (Chang et al., 2016; Thomas, 1975).

The earliest research on the water-entry problem is the study by Wood (1909), who observed 'Worthington jet' using photography technology. May and Woodhull (1948) experimentally and theoretically studied the change in the drag coefficient when a steel sphere enters the water. They observed that the drag coefficient was dependent on the Reynolds number (*Re*) and Froude number (*Fr*). Subsequently, May (1952) provided additional explanations and analysed regarding the changes in cavity volume, pressure and energy after a sphere enters the water.

On the basis of the previous studies, four cavity closure modes during the water entry of objects are summarised, namely, surface closure, deep closure, shallow closure and quasi-static closure. The cavity closure modes are found to be correlated with the Bond number and Weber number (Truscott et al., 2014). Later, the effects of the surface contact angle (Aristoff & Bush, 2009; Truscott et al., 2012), the initial rotational speed (Techet & Truscott, 2011), the geometric shape of the objects (Belden et al., 2023) and other parameters (Rabbi et al., 2020; Speirs et al., 2021) on the cavitation formation and development were investigated.

As cavity closure significantly affects the dynamics of the water entry of objects, the closure time and closure

NOMENCLATURE

D	sphere diameter	t_p	pinch-off time
d	inner diameter of sphere	H_p	depth of the cavity closure
D_d	horizontal diameter of deformed sphere	H	depth of the sphere's centre of mass
λ	sphere deformation scale	D_p	cavity's opening diameter at the water surface
v_0	impact velocity	ρ_s	sphere density
G	shear modulus	ρ_w	water density
z_b	lowest point displacement	λ_{PN}	maximum deformation coefficient for the Nth deformation cycle
T_{exp}	reference deformation period	D_{eff}	effective diameter
T_{model}	numerical model deformation period	T	deformation period
b	body force acting on the fluid	p	pressure
Σ	fluid stress tensor	f	porosity
μ	dynamic viscosity coefficient	E	internal energy per unit volume
v	poisson' s ratio	V	relative volume
t	time	I	identity tensor
$\vec{w}$	grid velocity	$\vec{u}$	fluid velocity
C_0	initial pressure	C_1	volume viscosity
C_2-C_6	constants	W	strain energy
I_1-I_3	invariants of the deformation tensor	F	deformation gradient

depth of the cavities were studied by many researchers. Aristoff et al. (2009) performed water-entry experiments using different solid spheres with varying densities, obtaining data results for cavity closure time, closure depth and gas volume inside the cavity at the closure moment. It was observed that for the densest rigid sphere (ρ = 7.86 g/cm^3), both the cavity pinch-off depth and the depth of the sphere's centre of mass at pinch-off exhibited a linear growth trend with $Fr^{1/2}$. With a decrease in sphere density, the depth of the sphere's centre of mass and the pinch-off depth no longer increased linearly with $Fr^{1/2}$.

Within the range of Re >> 1 and We >> 1, Duclaux et al. (2007) conducted experimental studies on the water entry of solid spheres and cylinders. They observed that for high Weber numbers and Reynolds numbers, the closure depth H/R_0 of the cavity was correlated with $Fr^{1/2}$, and for cylinders, H/R_0 was correlated with $Fr^{1/3}$. The cavity's opening diameter at the water surface, R/R_0, was correlated with $Fr^{1/4}$ for spheres, and for cylinders, R/R_0 was independent of Fr and R was close to R_0.

In subsequent studies on the low-Froude-number scope of cylinders, Gekle et al. (2006) found that the closure depth did not follow the expected $Fr^{1/3}$ power law. They observed that at low Froude numbers (Fr < 6), the closure depth of the cavity was proportional to $Fr^{1/10}$, and for Fr > 20, the closure depth was proportional to $Fr^{1/3}$. In the intermediate range, the closure depth of the cavity exhibited discrete points without a clear regular pattern.

Beyond sealing the cavity, when an object is in contact the water surface, the impact load becomes notably significant (Zhang et al., 2023), which may cause damage to biological organisms or mechanical components during this phase. Most studies of water entry do not consider the structural response and force-induced deformation of objects.

With the advancement of computational fluid dynamics technology, numerical simulation methods have been widely applied, driving further research into multiphase flow problems (Mohammadpour et al., 2013; Chabokpour & Azamathulla, 2022). Wang et al. (2013) conducted numerical simulations on the diving process of geese at different diving speeds and angles, revealing that oblique entries may cause damage to the necks of geese. This confirms that in reality, most geese opt for vertical entries for foraging. The numerical model also provides relevant design experience for biomimetics research.

Seddon and Moatamedi (2006) extensively discussed future research directions of object/water impact analysis. In their opinion, few efforts have been performed to devise solutions for three-dimensional objects or deformable structures. With the advancement of materials science and technology, hyperelastic materials have attracted significant attention in fields such as aerospace engineering because of their lightweight nature, ability to recover strain and high decomposition temperatures (Tang et al., 2017).

In recent years, Jandron et al. (2014) conducted numerical simulations and experiments on the oblique water entry of hyperelastic spheres using the Neo-Hookean hyperelastic model and a linear viscoelastic model with N = 3 Prony series. In the study, the numerical results demonstrated a strong agreement with the experimental results considering the sphere response and the size and shape of the cavity. However, more analysis and summary of the sphere's deformation and cavity motion patterns were not provided. Subsequently, Belden et al. (2016) conducted extensive experiments on the oblique water entry of hyperelastic spheres based on the work of Jandron et al. (2014). In the study, the entire process and mechanism of sphere deformation and jumping were given. In addition, the effects of the shear moduli, incident angles and velocities on the maximum deformation of the sphere and the impact angle formed when the sphere just hit the free surface were studied, and they obtained a parameter range in which the sphere jumped after hitting the water surface. However, these findings are primarily based on oblique water-entry processes.

In relation to the vertical water entry of hyperelastic solid spheres, Hurd et al. (2017) conducted experimental research on various shear moduli and diameters using high-speed cameras. They found that the sphere's deformation period measured in their experiment was slightly longer than that obtained by their developed numerical model. They attributed this difference to the additional mass during the sphere's water-entry process.

Furthermore, within the range of $Fr^{1/2}$ = 2–10, the closure time of the cavity showed a nearly linear relationship with $Fr^{1/2}$ for different shear moduli, but the closure time progressively reduced as the shear modulus of the sphere increased. In addition, they observed that when the shear modulus decreased, the speed fluctuations of the sphere became more pronounced. In this research, although the deformation of the spheres was observed, the stress distribution during the deformation period was not analysed.

To obtain a more detailed insight into the impact of various parameters on the deformation process of hyperelastic spheres, Yang et al. (2020b) conducted experiments and numerical simulations. Between rigid and hyperelastic spheres, they analysed the differences in structural responses and compared the changes in strain and kinetic energies. It was found that the strain energy of the hyperelastic sphere exhibited more pronounced fluctuations. By comparing the deformation of the sphere after water entry under different shear moduli and velocities, they observed that when the shear modulus increased, the deformation frequency of the sphere also increased and the peak of the deformation magnitude gradually decreased. As the velocity increased, the peak of the deformation magnitude of the sphere gradually increased but the sphere's deformation period did not change.

To understand the stress state and distribution during sphere deformation, Yang et al. (2020a) compared the stress variations between rigid and hyperelastic spheres. It was observed that the stress on the surface of the rigid sphere had no significant fluctuations and the ripples of the stress propagation on the elastic sphere were clearly visible. In their subsequent research (Yang et al., 2021a), they observed that with an increase in sphere density, the propagation speed of stress waves decreased, which led to an elongation of the deformation period. In 2021, Yang et al. (2021b) analysed the conditions and mechanisms of the nested cavity generated by the cyclical deformation of spheres after water entry.

The above studies focused on solid spheres, and no research work regarding hollow spheres has recently been reported. Compared with solid spheres, hollow spheres may undergo greater deformation in the water-entry process and it is necessary to study the deformation and stress change of hollow spheres during the water-entry process. This research on hollow structures can explore the deformation mechanisms after their immersion in water, and it is beneficial for solving many problems in aerospace and ocean engineering, such as transmedium aircraft and spacecraft (McGehee et al., 1959), water entry of ship's bows, emergency water landing of aircraft and water landing of re-entry capsules. In addition, the research of hollow spherical structures is also beneficial for the underwater robots, especially the head-like robots (Renda et al., 2015; Wehner et al., 2016; Tang et al., 2016).

In this paper, the water-entry process of solid and hollow hyperelastic spheres is numerically simulated for different initial velocities within low Froude numbers. The evolution of the cavity and deformation of the hyperelastic spheres are analysed under different conditions. In particular, the parameters at the time of cavity pinch-off are analysed. The difference in deformation and stress distribution between the solid and hollow spheres are compared.

2. THEORETICAL MODEL AND NUMERICAL METHODS

2.1 Governing Equation

In this paper, the arbitrary Lagrange–Euler (ALE) method (Candy et al., 2000) was used to handle the coupling between fluids and solid structure. The fluid is assumed to be incompressible. Therefore, the mass and momentum equations in the ALE form are represented as follows (Aquelet & Souli, 2004):

$$\nabla \cdot \vec{u} = 0 \tag{1}$$

$$\rho \frac{\partial \vec{u}}{\partial t} + \rho(\vec{u} - \vec{w}) \cdot \nabla \vec{u} = \vec{b} + \nabla \cdot \boldsymbol{\Sigma} \tag{2}$$

where $\vec{u}$ represents fluid velocity, $\vec{w}$ is grid velocity, t is time, $\vec{b}$ is the body force acting on the fluid and $\boldsymbol{\Sigma}$ is the fluid stress tensor:

$$\boldsymbol{\Sigma} = -p\boldsymbol{I} + \mu[\nabla \vec{u} + (\nabla \vec{u})^{\mathrm{T}}] \tag{3}$$

where p represents pressure, $\boldsymbol{I}$ denotes identity tensor and μ stands for the dynamic viscosity coefficient of the fluid.

2.2 Material Model and State Equation

In this paper, the Blatz–Ko model (Blatz & ko, 1962; Abeyaratne & Horgan, 1985) was selected as the material model of the hyperelastic sphere based on the research work by Lane et al. (2018), which can more exactly predict the stress of the material. The generalized Blatz-Ko strain energy function W is:

$$W = \frac{G(1-f)}{2}\left(\frac{I_2}{I_3} + \frac{1}{\alpha} I_3^{\alpha} - \gamma\right) + \frac{Gf}{2}\left(\frac{1}{\alpha} I_3^{-\alpha} + I_1 - \gamma\right) \tag{4}$$

where I_1, I_2 and I_3 represent the invariants of the deformation tensor; G denotes the shear modulus; f indicates the volume fraction of voids of the material; $\alpha = \nu/(1-2\nu)$, $\gamma = 1+1/\nu$, and ν is the Poisson's ratio of the material. And in this paper, the volume fraction of voids f was assumed to be 1.0. The Poisson's ratio ν of the material was 0.463. The stress of the solid material is calculated by:

$$\boldsymbol{\sigma} = \frac{G}{J}[\boldsymbol{B} - I_3^{-\alpha}\boldsymbol{I}] \tag{5}$$

where, $\boldsymbol{B} = \boldsymbol{F}\boldsymbol{F}^T$, $\boldsymbol{F}$ represents the deformation gradient; $J = \det(\boldsymbol{F})$.

Water and air were modelled using the Null material model and the pressure was calculated using the linear-polynomial state equation expressed in Eq. (6).

$$p = C_0 + C_1 V + C_2 V^2 + C_3 V^3 + (C_4 + C_5 V + C_6 V^2)E \quad (6)$$

where E represents the internal energy per unit volume, V denotes specific volume, C_0 is used to define the initial pressure, C_1 represents volume viscosity and C_2–C_6 are constants. The selection of the parameters of water and air was based on previous studies (Varas & López-Puente, 2009; Souli et al., 2014).

2.3 Numerical Method

We discretised the spatial domain using the finite element method based on Eulerian and Lagrangian descriptions for the fluid and solid phases, respectively. To couple the displacement at the interface between the fluid and solid phases, we used a penalty coupling algorithm with a coupling factor set to 0.1. In addition, we implemented the ALE advection method with second-order accuracy, specifically the Van Leer MUSCL scheme, to handle adaptive grid movement and compute the transport of variables at element centres. Finally, time discretization used second-order accuracy central differencing to approximate the time derivative terms in the partial differential equations.

2.4 Computational Domain and Parameters Setup

The fluid domain for the numerical simulation is depicted in Fig. 1(a). The meshes for the solid and hollow hemispheres are, respectively, shown in Fig. 1(b) and 1(c). In this study, the three-dimensional axisymmetric model of the sphere (xoz is the plane of symmetry, shown in Fig. 1(a)) was used. The size of the computational domain was $16D \times 8D \times 32D$. As for the selection of the computational domain, the size of the experimental water tank in the literature (Hurd et al., 2017) was referenced. Additionally, the selected size of the computational domain exceeds 10 times the sphere's diameter in all three directions, considering the three-dimensional axisymmetric model of the sphere. It is generally thought that the wall effects can be ignored when the computational domain is more than 10 times the characteristic size of the object being studied.

In the fluid domain, the upper part was the air and the lower part was the water. The heights of the air and water regions were $12D$ and $20D$, respectively. Except the symmetry boundary condition, the other boundary conditions were set as wall. The diameter of the sphere was D = 51 mm. The density of the sphere ρ_s was set to 1.07 g/cm^3, and the density of water ρ_w was 1.0 g/cm^3. At the initial time, the sphere was positioned above the water surface and then moved downwards in a certain velocity along the negative z-axis direction.

In Fig. 1(b) and 1(c), the meshes on solid and hollow hemispheres are given, respectively. In the simulation, the structured grids were adopted for the fluid domain and solid sphere. For the fluid domain, grid refinement was conducted near the free surface and in the region where the sphere passed through.

3. VALIDATION OF MESH INDEPENDENCE AND NUMERICAL METHODS

In this paper, grid independence verification was first conducted. The fluid domain and the meshes on a semisphere are shown in Fig. 1. In this part, four different grid numbers, namely, 1.2 million, 2.2 million, 3 million and 4 million, were chosen for the verification. These four grid numbers corresponded to mesh sizes in the refined region of 4.3, 2.9, 2.1 and 1.6 mm, respectively.

Figure 2 illustrates the variation of the sphere's deformation parameter λ with time for different grid numbers. The ordinate, λ, in Fig. 3 is defined as D_d/D, where D is the diameter of the sphere before deformation and D_d is the transverse dimension of the deformed sphere. The schematic of the sphere's deformation during the water-entry process is depicted in Fig. 3. When $\lambda > 1$, the sphere experienced transverse compression in the xoz plane; when $\lambda < 1$, the sphere underwent longitudinal stretching; and if $\lambda = 1$, the sphere returned to its original shape. In addition, two vertical lines were added in Fig. 2. The interval between these two vertical lines represented one deformation period T, during which the sphere underwent transverse compression and longitudinal stretching.

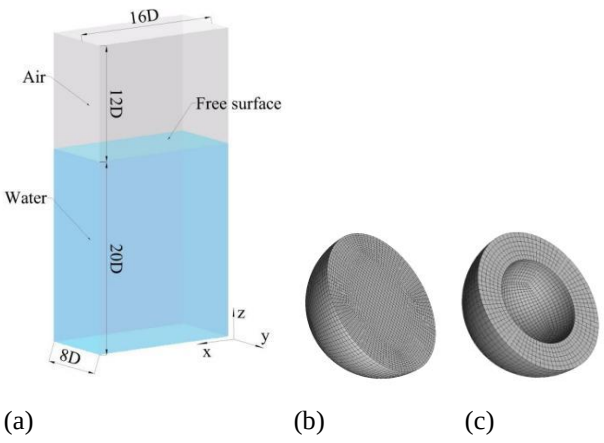

Fig. 1 Computational domain and meshes. (a) Fluid domain, (b) mesh on the solid hemisphere and (c) mesh on a hollow hemisphere

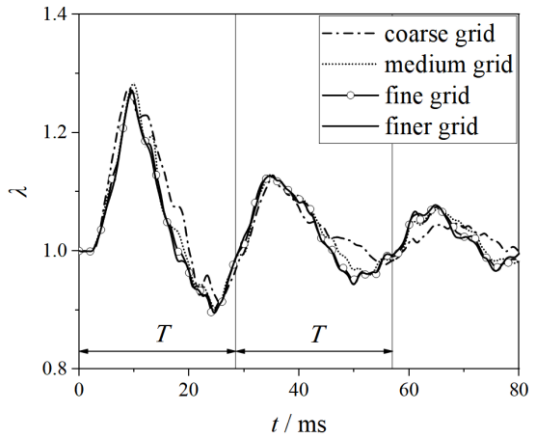

Fig. 2 Comparison of λ variations with time between the simulation results and experimental data for different mesh numbers

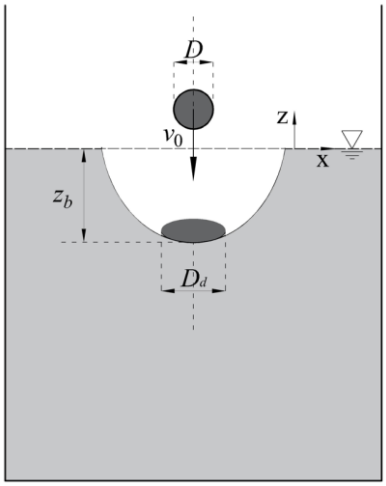

Fig. 3 Schematic of the parameters of the sphere deformation in the motion process

As shown in Fig. 2, the results obtained with the coarse grid showed obvious differences near t = 50 ms compared with the other three cases. The result with the medium grid showed slight variations compared with that with the fine mesh, whereas the result difference between the fine mesh and finer mesh was negligible. Therefore, considering both computational cost and numerical accuracy, the following simulations were conducted using the fine grid, i.e. with 3 million grid elements. For the hollow sphere investigated later, the same element size as the solid sphere, i.e. 2 mm, was chosen.

To validate the physical models and numerical methods, Fig. 4 provides the comparison of the evolution of the cavity profile between the numerical results and experimental data (Hurd et al., 2017). Time was non-dimensionalised by the deformation period T of the sphere. In Hurd's experiment, the diameter of the solid sphere was 51 mm, with a shear modulus of 6.7 kPa, a density of 1.07 g/cm³ and an initial water-entry velocity of

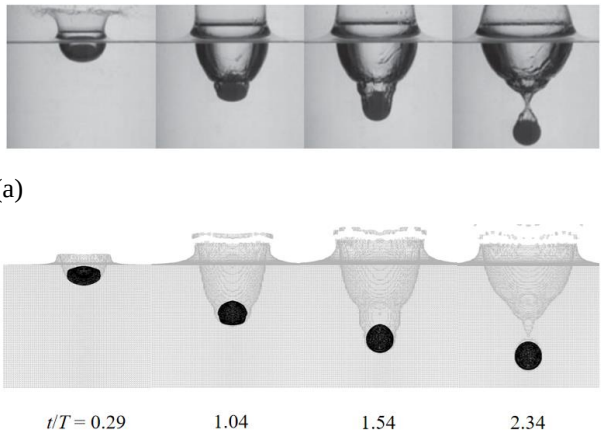

(a)

(b)

Fig. 4 Comparison of the cavity contour at different times. (a) Experimental data (Hurd et al., 2017). (b) Numerical results

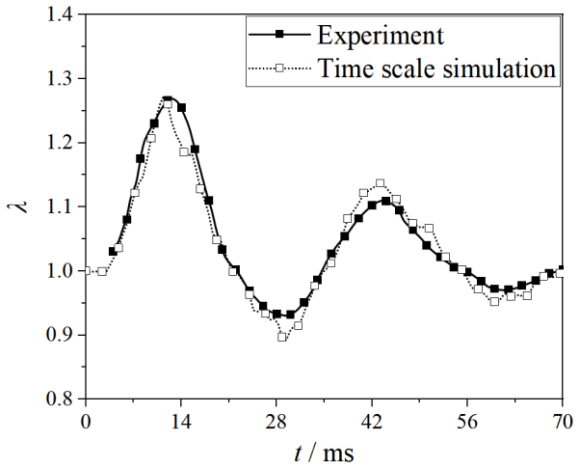

(a)

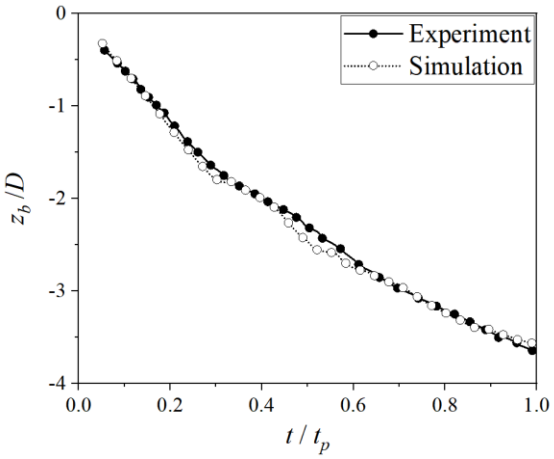

(b)

Fig. 5 Changes in the lateral deformation parameter λ and submersion depth z_b of the sphere with time

5.3 m/s. As shown in Fig. 4, the height of the water crown splashed by the entering sphere in the experiment was slightly higher than that in the numerical simulation but the difference in the diameters of the water crown between the experiment and simulation was not obvious. In addition, the cavity contour, cavity size and deformation of the sphere obtained from the simulation all approximately matched those in the experiment. At t/T = 0.29, the sphere just entered the water and was in the phase of compression deformation. Subsequently, the sphere gradually returned to its original size. Following that, the vertical dimension of the sphere increased, indicating the stretching phase in the vertical direction. At t/T = 1.04, the cavity exhibited a phenomenon known as nested cavities (Yang et al., 2021b). At t/T = 1.54, the sphere was slightly stretched in the perpendicular direction and the surface curvature of the sphere at the lower part was smaller than that at the upper one. At this time, the cavity profile was presented in a three-segment distribution. Finally, at t/T = 2.34, the cavity was pinched off.

Figures 5(a) and 5(b) depict the variations of the lateral deformation parameter λ and the submersion depth z_b of the sphere with time, respectively. Here, z_b represents the position coordinate of the sphere's bottom. The

position of the water surface is defined as $z = 0$, and the z-axis is negative downwards. The schematic of λ and z_b is already shown in Fig. 3.

As shown in Fig. 5(a), the lateral dimension of the sphere increased, i.e. $\lambda > 1$, as the sphere just entered the water. When λ increased to approximately 1.27, the deformation ceased and the sphere began to recover its original shape. After λ decreased to 1.0, the lateral dimension of the sphere continued to decrease, indicating the elongation in the vertical direction. Notably, the percentage of the vertical elongation was smaller than that of the lateral compression. Subsequently, the sphere underwent another cycle, i.e. first compression and then stretching. The fluctuation magnitude of λ in the second deformation cycle was significantly smaller than that in the previous cycle. Overall, the numerical results closely matched the experimental data, as shown in the figure.

Here, it should be noted that the time scale in Fig. 5(a) for numerical simulation has been adjusted. In the numerical simulation, the sphere's deformation period was slightly shorter than that of the experimental results reported by Hurd et al. (2017). A similar observation was made in the numerical simulation by Hurd et al. (2017), who attributed it to the additional mass of the sphere, leading to a scaling of the numerical results. In this study, we used a scaling factor of $T_{exp}/T_{model} = 1.15$.

Figure 5(b) shows the variation of the submersion depth z_b of the sphere with time. The horizontal axis is non-dimensionalised by the pinch-off time t_p of the cavity. It can be observed the numerical results closely matched the experimental data.

Based on the above validation of grid independence and numerical methods, the water-entry process for the solid and hollow spheres was investigated by considering the interaction between the fluid and sphere.

4. NUMERICAL RESULTS AND DISCUSSIONS

In this paper, the water-entry process for solid and hollow spheres was studied. In addition, the effect of the sphere velocity on the water-entry process and the deformation of the sphere was investigated.

4.1 Water entry of the Solid Sphere with Different Speeds

The water-entry process of a solid sphere with five different velocities (v_0 = 1.3, 2.3, 3.3, 4.3 and 5.3 m/s; Fr = 3.4–56.2) was simulated. The sphere diameter D was 51 mm, and the density and shear modulus were 1.07 g/cm^3 and G = 6.7 kPa, respectively. Correspondingly, the Froude numbers (Fr) expressed by Eq. (7) for the five conditions were 3.4, 10.6, 21.8, 37.0 and 56.2, respectively.

$$Fr = v_0^2 / (gL) \tag{7}$$

where g represents the acceleration due to gravity and L represents the characteristic length of the object. In this paper, the characteristic length L of the solid sphere is the diameter D of the sphere.

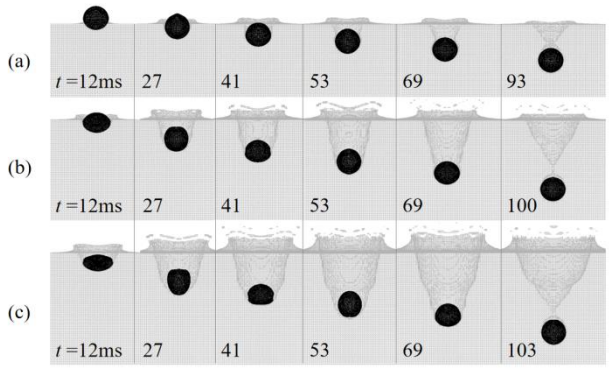

Fig. 6 Evolution process of the cavity of the solid sphere while entering the water with different Froude numbers. (a) *Fr* = 3.4, (b) *Fr* = 21.8 and (c) *Fr* = 56.2

In Fig. 6, the evolution process of the cavity of the solid sphere during the water-entry process with different Froude numbers (Fr = 3.4, 21.8, 56.2) is presented. The time for the first five images among Fig. 6(a), 6(b) and 6(c) is the same with each other, which is varied from t = 12 to 69 ms in Fig. 6(a), 6(b) or 6(c). However, the time for the last image was different, representing the closure time of the cavity for the corresponding condition. The closure times for the condition of Fr = 3.4, 21.8 and 56.2 were 93, 100 and 103 ms, respectively.

As shown in Fig. 6(a), when Fr = 3.4 (v_0 = 1.3 m/s), no cavity was visible around the sphere at t = 12 or 27 ms for the condition of Fr = 3.4. The cavity appeared at t = 41 ms, but the contact line between the sphere and cavity was located behind the hemispherical part of the sphere. Subsequently, with the passage of time, the contact line continued to move backward (observable at t = 53 and 59 ms). Later, when the sphere descended to a certain depth, the cavity rapidly contracted because of the water pressure and the Venturi effect, resulting in the pinch-off of the cavity. Sphere deformation was relatively not obvious.

As the Froude number increased, the size of the cavity increased and the deformation of the sphere was more pronounced, which will be discussed further later.

In addition, at t = 41 ms for the condition of Fr = 21.8, the cavity profile was not smooth but exhibited fluctuations. As time progresses, the fluctuations propagated along the cavity wall, becoming less pronounced.

For the condition of Fr = 56.2 (Fig. 6(c)), the fluctuation on the cavity wall was more pronounced than that for the other conditions. This is attributed to the fact that the sphere with a higher speed had greater kinetic energy, resulting in greater impact loading acting on the sphere (Zhang et al., 2023). For the condition of a bigger Froude number, because of the bigger impact loading on the sphere with the same shear modulus, the corresponding deformation increased.

When the sphere began to enter the water, the sphere was first compressed. The extent of the compression for Fr = 56.2 was greater than that for Fr = 21.8. Thus, the diameter of the cavity for Fr = 56.2 was bigger. After reaching the maximum lateral compression, the sphere

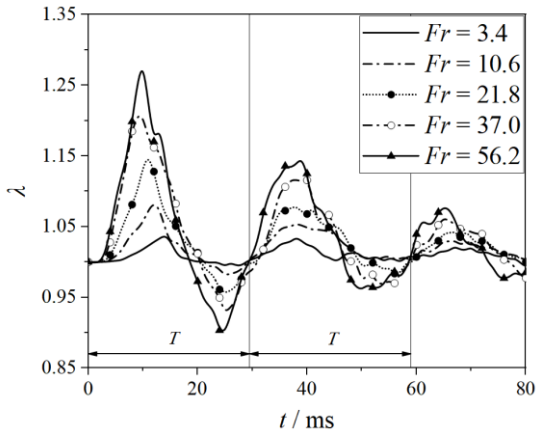

Fig. 7 Variation of the lateral deformation parameter λ of the solid sphere with time for different cases

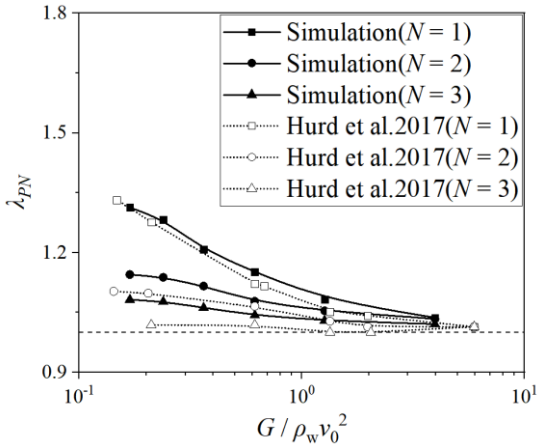

Fig. 8 Relationship between the deformation parameter λ_{PN} and the dimensionless parameter $G/\rho_w v_0^2$

underwent a transition to longitudinal stretching, transforming from a laterally flattened sphere to a longitudinally elongated one. In this process, the sphere opened a smaller cavity downwards because of longitudinal stretching, possibly contributing to the subsequent formation of nested cavities. Yang et al. (2021b) explained that the formation conditions of the nested cavities involved a specific impact velocity and a certain amount of deformation.

To quantitatively compare the deformation of the sphere, Fig. 7 illustrates the variation of the lateral deformation parameter λ over time for different Froude numbers. When $\lambda > 1$, the sphere underwent a lateral compression. Conversely, the sphere experienced longitudinal stretching when $\lambda < 1$. It is evident from Fig. 7 that the sphere underwent periodic cycles of compression and stretching. Both the magnitude of the maximal compression and stretching appeared at the first period, and subsequently, the magnitude of the maximum deformation gradually decreased. Eventually, the magnitude of the deformation tended to be 1. This is attributed to gradual dissipation of the energy of the sphere during the downwards movement.

In addition, as observed in Fig. 7, the peak value of the deformation coefficient of the sphere increased with *Fr*. Furthermore, the deformation period of the sphere did not change for five different conditions. That is, the velocity variation within this range did not alter the sphere's deformation period. This finding is in agreement with the conclusion obtained by Yang et al. (2020b).

Figure 8 illustrates the relationship between the deformation coefficient λ_{PN} and the dimensionless parameter $G/\rho_w v_0^2$. Here, λ_{PN} represents the maximum lateral deformation during the *N*th deformation period. Because of the gradual reduction of the sphere deformation, only the variation of λ_{PN} for the first three deformation cycles was presented in the figure, along with a comparison with the experimental results of Hurd et al. (2017).

As shown in Fig. 8, the overall trends of the three datasets were generally consistent and the maximum deformation was eventually approaching 1. During the first deformation cycle, the deformation coefficient from the numerical simulations closely matched the experimental data. In the second and third deformation cycles, λ_{PN} obtained from the numerical calculations was slightly larger than that in the experiment.

With the downwards movement of the sphere, the pinch-off of the cavity or cavity closure will occur. The cavity closure will influence the dynamic characteristics of the sphere. Figure 9 illustrates the relationship between the pinch-off time t_p of the cavity and *Fr*. The ordinate was dimensionless using D/v_0. Both axes were presented in logarithmic scales to provide a more direct understanding of the relationship between the ordinate and *Fr*. Consequently, each set of the data in the figure was fitted to obtain the slope. Meanwhile, the outcomes were compared with the experimental data in the studies by Hurd et al. (2017) and Duclaux et al. (2007). It should be noted that the physical parameters of the sphere in this paper were the same with those in Hurd et al. (2017) but were not different from those in Duclaux et al. (2007). In the investigation of Duclaux et al. (2007), the density was 2.487 g/cm^3.

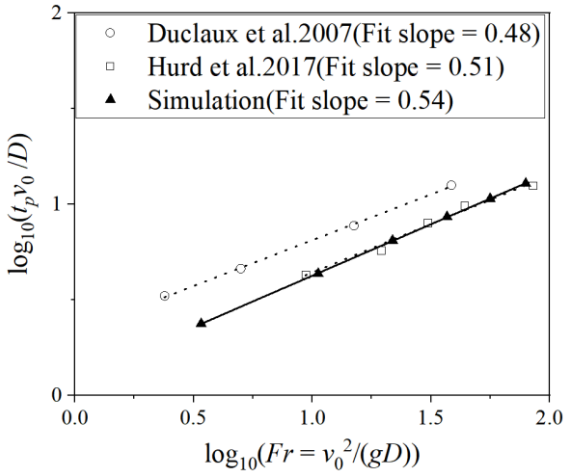

Fig. 9 Relationship between the cavity closure time t_p and *Fr*

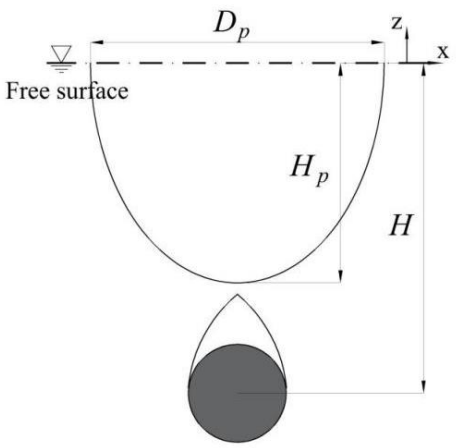

Fig. 10 Schematic of H_p, H and D_p at the time of cavity closure

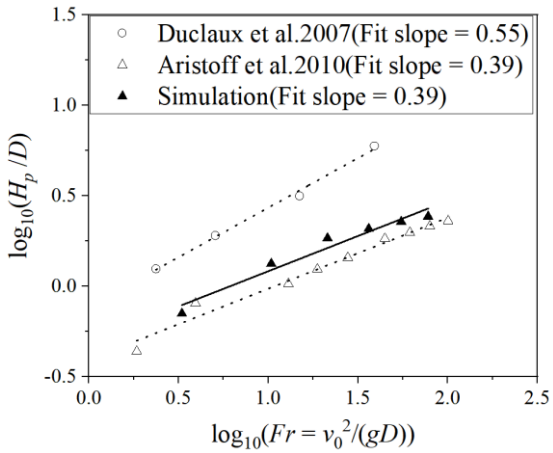

Fig. 11 Relationship between H_p and Fr at $t = t_p$

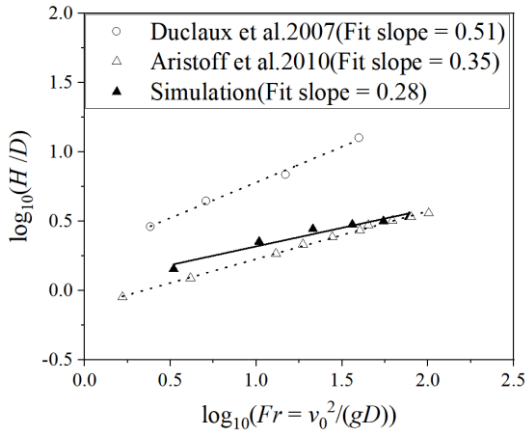

Fig. 12 Relationship between H and Fr at $t = t_p$

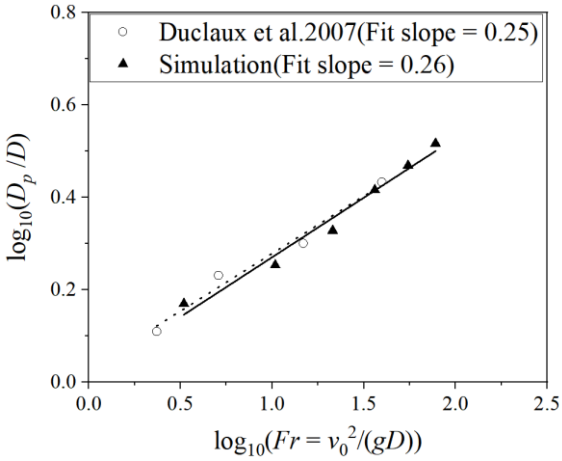

Fig. 13 Relationship between D_p and Fr at $t = t_p$

As shown in Fig. 9, the slopes of the three datasets were quite close and the closure time of the cavity was linearly related to approximately $Fr^{1/2}$. Furthermore, the simulated results aligned well with the experimental measurement from the study by Duclaux et al. (2007). The difference between the simulation results in this paper and that by Duclaux et al. (2007) may be due to the difference in density.

To further investigate cavity closure, the depth of the cavity closure (H_p), the depth of the sphere's centre of mass (H) and the cavity's opening diameter at the water surface (D_p) at the moment of cavity closure will be analysed. Figure 10 presents the schematic of these three parameters. In Figs. 11, 12 and 13, the variations in H_p, H and D_p with the Froude number are given, respectively.

Figure 11 depicts the relationship between the depth of the cavity closure and Fr, with comparisons to the experimental data from Aristoff et al. (2009) (ρ = 1.14 g/cm³) and Duclaux et al. (2007) (ρ = 2.487 g/cm³). We can see that the simulation results were closer to the experimental data of Aristoff than that to those of the study by Duclaux et al. (2007). The fitting slope of the simulation results was the same with that in the study by Aristoff et al. (2009). In Fig. 12, the change in H in the simulations was still closer to the data in Aristoff et al. (2009) than that in Duclaux et al. (2007). However, in Fig. 13, as for the opening diameter of the cavity in the free surface at the moment of cavity closure, the simulation results aligned well with those in the study by Duclaux et al. (2007), considering whether it is slope or specific value.

Figure 14 illustrates the variation in the depth of the sphere with time. The horizontal axis is dimensionless using D/v_0, and the vertical axis, z_b, is dimensionless using the sphere diameter. The definition of z_b can be referenced in Fig. 3. It can be observed that when Fr = 3.4 and 10.6, the curve of z_b was relatively smooth, exhibiting a mostly linear trend. When Fr = 37.0, a slight fluctuation appeared in the vicinity of 3 (tv_0/D). As Fr increased to 56.2, the fluctuation became more pronounced. The reason of the fluctuation can be explained as follows.

To explain the reason of the curve fluctuation in Fig. 14, the stress distributions on the sphere at different times were observed. In Fig. 14, under the condition of Fr = 56.2, the stress distributions for three typical positions were given, which were marked with a red triangle, circle and square.

At the time marked by the red circle, the maximal stress appeared at the top of the sphere. At this moment,

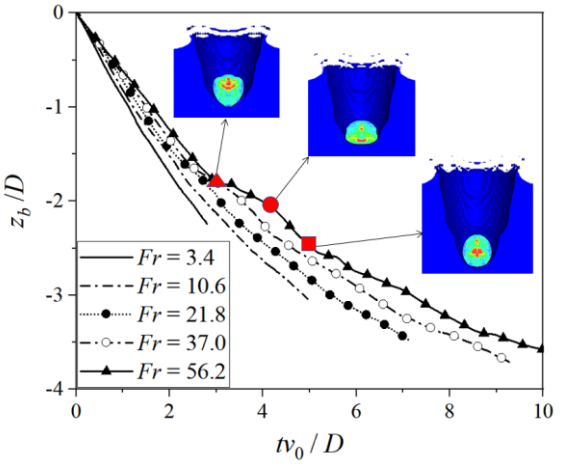

Fig. 14 Variation of the sphere depth z_b with time

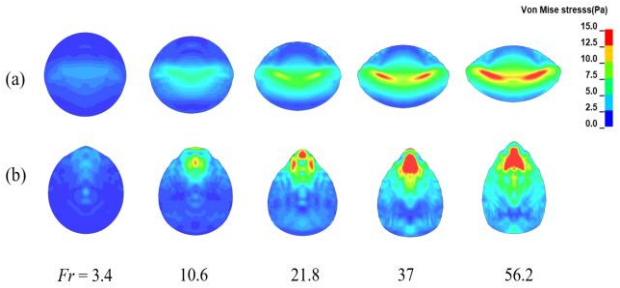

Fig. 15 Stress distribution in the xoz cross-section for solid spheres under different conditions, (a) maxial lateral compression, (b) maximal longitudinal stretch

the sphere just finished the stretching process and just began the process of lateral compression. At the red circle, the sphere reached its maximal lateral compression and the stress at the sphere bottom was bigger. This indicates that during this period the internal stress in the sphere shifted from top to bottom, suggesting that the bottom of the sphere was compressed more significantly compared with the top. During this compression process, the resistance coefficient gradually increased, accompanied with the growth of the sectional area of the sphere. Thus, under the combined effects of the increased drag and sphere lateral compression, the change in z_b became slow and at the red circle, the change in z_b was the smallest. After this, the sphere began to return to its original shape. At the time of the red square, the stress at the bottom of the sphere was released and the maximal stress appeared in the middle of the sphere. During the process from the red circle to the red square, the sectional area decreased and thus the drag correspondingly decreased. Accompanied with the recovery of the sphere shape, the change in z_b increased. Therefore, it may be concluded that the deformation of the sphere caused the curve fluctuation of z_b. With the increase in *Fr*, the deformation of the sphere increased and the curve fluctuation of z_b increased.

Figure 15 shows the stress distribution in the xoz cross-section for solid spheres under different conditions. In Fig. 15(a), the sphere is in a state of maximal lateral compression for every condition, while Fig. 15(b) corresponds to the state of maximal longitudinal stretch. The unit of the stress was Pa. It can be observed that the maximal stress appears in the middle of the sphere in Fig. 15(a). However, in Fig. 15(b), the maximal stress occurs in the top region of the sphere.

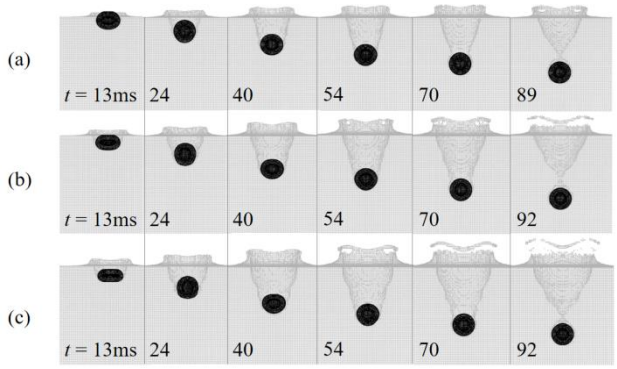

Fig. 16 Evolution process of the cavity of the hollow sphere while entering the water with different Froude numbers. (a) *Fr* = 23.6, (b) *Fr* = 40.1 and (c) *Fr* = 61

4.2 Water entry of the Hollow Sphere with Different Speeds

In this study, the water-entry process of a hollow sphere was also investigated. In the numerical simulations, the inner diameter (d) of the sphere was 31 mm and the outer diameter (D) was 51 mm. The shear modulus (G) was 24 kPa. The velocity range for the hollow sphere was the same as that for the solid one, i.e. ranging from 1.3 to 5.3 m/s. The corresponding Froude number was in the range of 3.7–61. It should be noted that the effective diameter of the sphere ($D_{eff} = (D_3\text{-}d_3)^{1/3}$) in the calculation of *Fr* was used.

Figure 16 illustrates the evolution process of the cavity of the hollow ball while entering the water with different Froude numbers.

The closure times (t_p) for *Fr* = 23.6, 40.1 and 61 were 89, 92 and 92 ms, respectively. It can be observed from the figure that a slight lateral elongation of the sphere was noticeable at t = 13 ms under the condition of *Fr* = 23.6, but the deformation was smaller compared with the other two conditions. For the case of *Fr* = 40.1, both the top and bottom parts of the sphere appeared flattened at t = 13 ms, which was different from the deformation pattern observed in the solid sphere. When *Fr* was increased to 61, the lateral elongation of the sphere was the biggest at t = 13 ms. In addition, the cavity size increased with the Froude number, which was similar to that for the solid sphere.

Similarly, Fig. 17 depicts the variation of the deformation coefficient (λ) with time for hollow spheres under various Froude numbers. It can be seen that the amplitude of the deformation coefficient was minimal at *Fr* = 3.7. As the initial speed of the sphere increases, the deformation became more obvious. However, because of the energy loss, the deformation gradually diminished, resulting in the convergence of the deformation levels among different conditions.

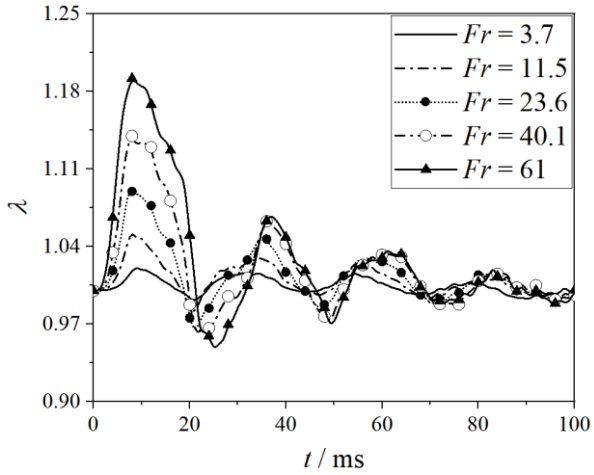

Fig. 17 Variation of the lateral deformation parameter λ of the hollow sphere with time for different cases

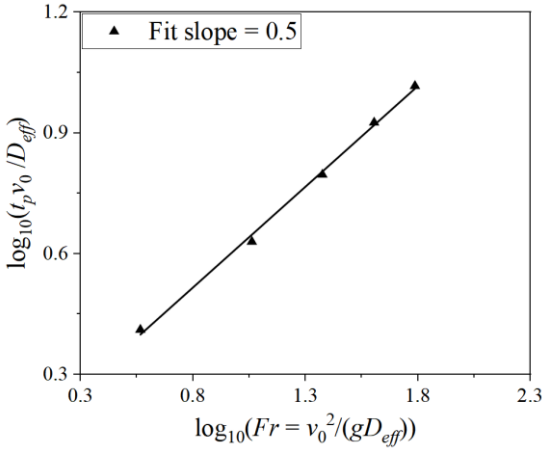

Fig. 18 Relationship between t_p and Fr

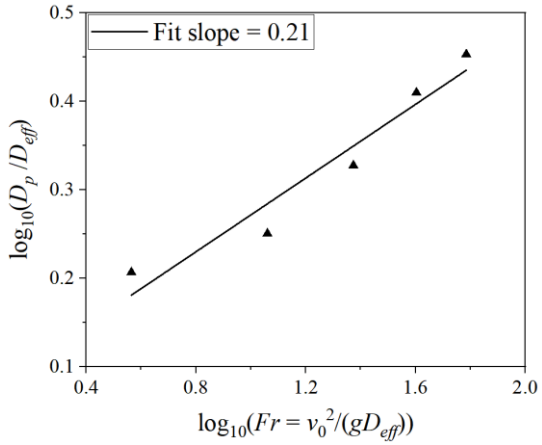

Fig. 19 Relationship between D_p and Fr at $t = t_p$

Figures 18–21 present the changes in t_p, D_p, H_p and H with the Froude number for the hollow sphere when the cavity was pinched off. By comparing Figs. 18–21, we can observe that the dimensionless pinch-off time, water surface opening diameter, pinch-off depth of the cavity,

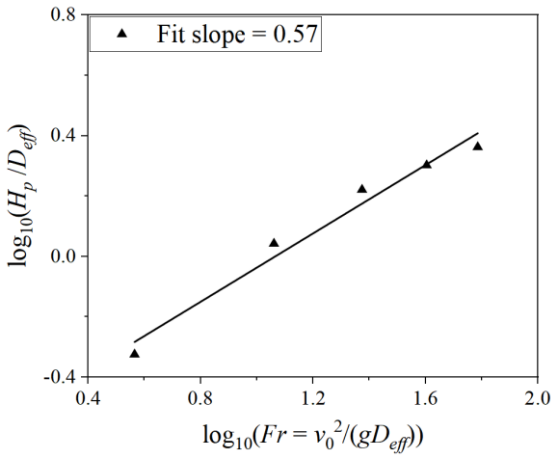

Fig. 20 Relationship between H_p and Fr at $t = t_p$

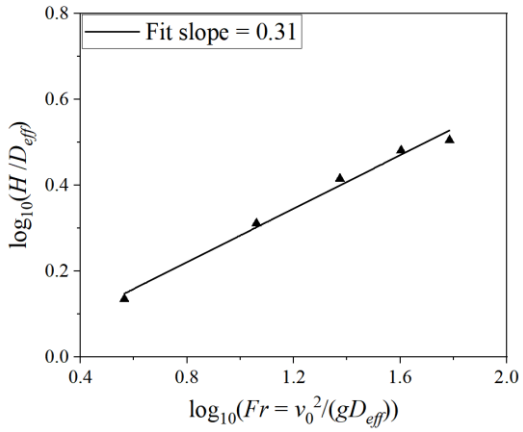

Fig. 21 Relationship between H and Fr at $t = t_p$

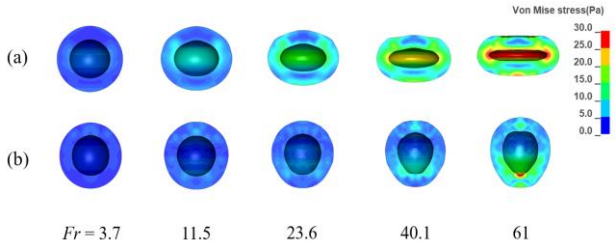

Fig. 22 Stress distribution in the xoz cross-section for hollow spheres under different conditions, (a) maxial lateral compression, (b) maximal longitudinal stretch

and sphere centroid depth were all positively correlated with Fr in certain power functions. This trend is consistent with the variation trend of cavity pinch-off parameters for different velocity solid spheres. However, the parameter most affected by Fr in the cavity fracture parameters was the dimensionless pinch-off depth, followed by the dimensionless pinch-off time, sphere centroid depth and water surface opening diameter.

Figure 22 shows the stress distribution in the xoz cross-section for hollow spheres under different conditions. In Fig. 22(a), the sphere is in a state of maximal lateral compression for every condition, while

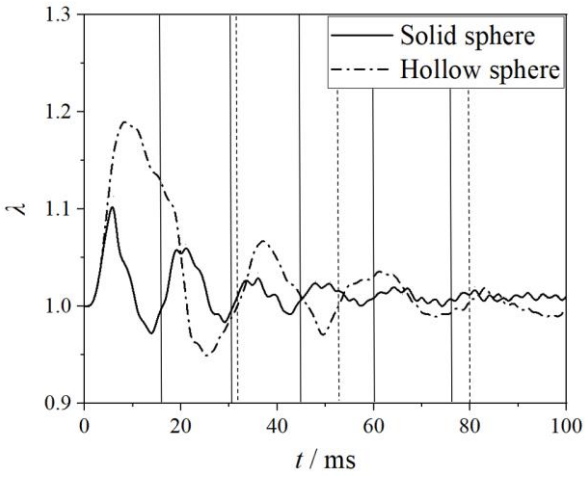

Fig. 23 Comparison of λ between the solid and hollow spheres

Figure 22(b) corresponds to the state of maximal longitudinal stretch. The unit of the stress was Pa. It can be observed that the maximal stress appears at the two ends of the inner edge of the sphere in Fig. 22(a). However, the maximal stress appears at the lower end of the inner edge of the sphere.

4.3 Comparison of Water-Entry Processes Between Solid and Hollow Spheres

To clearly and quantitatively compare the differences between the solid and hollow spheres, Fig. 23 provides a comparison of the deformation coefficients during the water-entry processes of a hollow sphere (inner diameter d = 31 mm; outer diameter D = 51 mm) and a solid sphere (outer diameter D = 51 mm). Both spheres had an initial velocity of 5.3 m/s and a shear modulus of 24 kPa.

In Fig. 23, several solid and dashed lines were added to identify the deformation periods of the solid and hollow spheres. We can see in Fig. 23 that the amplitude of the deformation coefficient of the hollow sphere was significantly larger and the deformation period of the hollow sphere was longer than that of the solid one. Here, the first deformation period of the hollow sphere is about 1.5 times that of solid sphere.

To explore the difference of the phenomena and data between the hollow and solid spheres during the water-entry process, the stress distributions of the xoz cross-sections of both the hollow and solid spheres at different times were compared. Figure 24 presents the xoz cross-sections of the solid and hollow spheres. The unit of the stress was Pa.

As shown in Fig. 24(a), the stress in the middle was higher than that in the other part at t = 5 ms. At this time, the sphere was just in the state of maximal lateral compression. Then, with time, the sphere underwent stretching in the perpendicular direction and the high stress zone shifted upwards. When the sphere reached its maximal longitudinal stretching (t = 12 ms), the high stress zone appeared at the upper part of the sphere. Later, the sphere experienced another deformation cycle and the stress underwent a corresponding shifting cycle.

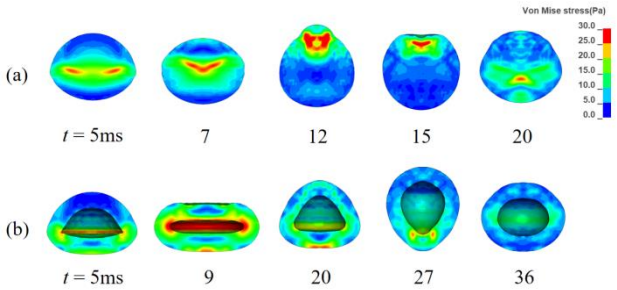

Fig. 24 Stress comparison of solid and hollow spheres at different times after entering the water

In Fig. 24(b), at t = 5 ms, the hollow sphere was compressed. We can see that the lower part was more severely compressed than the upper part. Then, the hollow sphere was continuously compressed. At t = 9 ms, the upper and lower parts of the sphere were flat. At this time, the maximal stress was higher than that at t = 5 ms. At t = 20 ms, the sphere began to stretch along the vertical direction. It should be noted that stretching started from the upper half of the hollow sphere. The hollow sphere had an approximately triangular shape. At t = 27 ms, the lower part of the sphere also underwent stretching. Subsequently, the hollow sphere was compressed again.

5. CONCLUSIONS

In this paper, the water-entry process of solid and hollow hyperelastic spheres was numerically simulated for different initial velocities within low Froude numbers. The coupling of the sphere and fluid was handled using the ALE method. The evolution of the cavity and deformation of the hyperelastic spheres were analysed under different conditions. In particular, the parameters at the moment of cavity pinch-off were analysed and compared with several published data. Meanwhile, the differences in the deformation and stress distribution between solid and hollow spheres were also compared. The following conclusions can be drawn:

(1) The size of the cavity and fluctuation on the cavity profile increased with Fr for the solid sphere. The closure time and closure depth of the cavity also increased with Fr. For the solid sphere, the closure time was proportional to $Fr^{1/2}$ and the closure depth was proportional to $Fr^{2/5}$ under the investigated cases in this paper.

(2) For the hollow sphere, the change trends of the size of the cavity and fluctuation on the cavity profile were the same with those for the solid sphere. The closure time and closure depth of the cavity for the hollow sphere also increased with Fr. The closure time for the hollow sphere was proportional to $Fr^{1/2}$, which was the same as that for the solid sphere. The closure depth for the hollow sphere was proportional to $Fr^{3/5}$, which was different from that for the solid one.

(3) While entering the water, both the solid and hollow spheres experienced the periodic deformation process of first lateral compression and then longitudinal stretching. The deformation amplitude gradually decreased with time for every condition. However, the

difference lies in the fact that during the initial stretching process, the top and bottom of the hollow sphere were stretched successively, and in the case of the solid sphere, only the top underwent stretching.

(4) Within the investigated low Froude numbers, whether for the solid or hollow spheres, the deformation amplitude increased with the Froude number. However, the deformation period remained nearly the same for different conditions.

(5) For the solid sphere, the high stress zone was located in the middle when it reached its maximal lateral compression. The high stress zone was in the upper part of the sphere when the sphere was in its maximal longitudinal stretching. The change in the stress distribution for the hollow sphere was more complex than that for the solid one.

In the future, the experiments of deformable hollow spheres entering water will be conducted in order to further investigate and understand the cavity evolution, the sphere deformation and the coupling effects between the fluid and solid structure. The experimental cases for hollow spheres will provide valuable data for the above and future numerical simulations.

ACKNOWLEDGEMENTS

The National Natural Science Foundation of China (Grant No. U21A20126) and Natural Science Foundation of Zhejiang Province, China (Grant No. LQ13A020005 and LY17E060006) funded this research.

CONFLICT OF INTEREST

The authors have no conflicts of interests to disclose.

AUTHORS CONTRIBUTION

L. Zhang: Conceptualization, methodology, resources, supervision; **R. Xie:** validation, formal analysis, writing, editing; **H. Jia:** Conceptualization, methodology, formal analysis, writing, supervision. All authors have read and agreed to the manuscript in its published version.

REFERENCES

Abeyaratne, R., & Horgan, C. O. (1985). Initiation of localized plane deformations at a circular cavity in an infinite compressible nonlinearly elastic medium. *Journal of Elasticity*, *15*, 243–256. https://doi.org/10.1007/bf00041423

Aquelet, N., & Souli, M. (2004, 25 July). *Fluid-structure coupling in a water-wedge impact problem*. [ASME/JSME 2004 Pressure Vessels and Piping Conference–San Diego, California, USA]. Emerging Technology in Fluids, Structures, and Fluid Structure Interactions. (pp. 91–99). https://doi.org/10.1115/PVP2004-2887

Aristoff, J. M., & Bush, J. W. (2009). Water entry of small hydrophobic spheres. *Journal of Fluid Mechanics*, *619*, 45–78. https://doi.org/10.1017/s0022112008004382

Aristoff, J. M., Truscott, T. T., Techet, A. H., & Bush, J. W. (2009). The water entry of decelerating spheres. *Physics of Fluids*, *22*, 032102. https://doi.org/10.1063/1.3309454

Belden, J. L., Hurd, R. C., Jandron, M. A., Bower, A. F., & Truscott, T. T. (2016). Elastic spheres can walk on water. *Nature Communications*, *7*, 10551 https://doi.org/10.1038/ncomms10551

Belden, J. L., Speirs, N. B., Hellum, A. M., Jones, M., Paolero, A. J., & Truscott, T. T. (2023). Water entry of cups and disks. *Journal of Fluid Mechanics*, *963*, A14. https://doi.org/10.1017/jfm.2023.330

Blatz, P. J., & Ko, W. (1962). Application of finite elastic theory to the deformation of rubbery materials. *Transactions of The Society of Rheology*, *6* (1): 223–252. https://doi.org/10.1122/1.548937

Candy, E. G., Kirk, N. E., & Murrell, P. J. (2000). Airframe water impact analysis. *International Journal of Crashworthiness*, *5*, 51–62. https://doi.org/10.1533/cras.2000.0123

Chabokpour, J., & Azamathulla, H. M. (2022). Numerical simulation of pollution transport and hydrodynamic characteristics through the river confluence using FLOW 3D. *Water Supply*, *22*(10), 7821-7832. https://doi.org/10.2166/ws.2022.237

Chang, B., Croson, M., Straker, L., Gart, S. W., Dove, C., Gerwin, J. A., & Jung, S. (2016). How seabirds plunge-dive without injuries. *Proceedings of the National Academy of Sciences*, *113*(43), 12006–12011. https://doi.org/10.1073/pnas.1608628113

Duclaux, V., Caille, F., Duez, C., Ybert, C., Bocquet, L., & Clanet, C. (2007). Dynamics of transient cavities. *Journal of Fluid Mechanics*, *591*, 1–19. https://doi.org/10.1017/S0022112007007343

Gekle, S., van der Bos, A., Bergmann, R., van der Meer, D., & Lohse, D. (2006). Noncontinuous froude number scaling for the closure depth of a cylindrical cavity. *Physical Review Letters*, *100*(8), 084502. https://doi.org/10.1103/physrevlett.100.084502

Hurd, R. C., Belden, J. L., Jandron, M. A., Tate Fanning, D., Bower, A. F., & Truscott, T. T. (2017). Water entry of deformable spheres. *Journal of Fluid Mechanics*, *824*, 912–930. https://doi.org/10.1038/ncomms10551

Jandron, M. A., Hurd, R. C., Belden, J. L., Bower, A. F., Fennell, W. A., & Truscott, T. T. (2014). *Modeling of hyperelastic water-skipping spheres using abaqus/explicit*. SIMULIA Community Conference.

Kross, D. A., Kiefling, L. A., Murphy, N. C., & Rawls, E. A. (1983, May 02– May 04). *Space Shuttle solid rocket booster initial water impact loads and dynamics-Analysis, tests, and flight experience*. [American Institute of Aeronautics and Astronautics 24th Structures, Structural Dynamics and Materials

Conference–Lake Tahoe]. 24th Structures, Structural Dynamics and Materials Conference. https://doi.org/10.2514/6.1983-956

Lane, B. A., Harmon, K. A., Goodwin, R. L., Yost, M. J., Shazly, T., & Eberth, J. F. (2018). Constitutive modeling of compressible type-I collagen hydrogels. *Medical Engineering & Physics*, *53*, 39–48. https://doi.org/10.1016/j.medengphy.2018.01.003

Machovsky-Capuska, G. E., Howland, H. C., Raubenheimer, D., Vaughn-Hirshorn, R., Würsig, B., Hauber, M. E., & Katzir, G. (2012). Visual accommodation and active pursuit of prey underwater in a plunge-diving bird: the Australasian gannet. *Proceedings of the Royal Society B: Biological Sciences*, *279*(1745), 4118-4125. https://doi.org/10.1098/rspb.2012.1519

May, A. (1952). Vertical entry of missiles into water. *Journal of Applied Physics*, *23*, 1362–1372. https://doi.org/10.1063/1.1702076

May, A., & Woodhull, J. C. (1948). Drag coefficients of steel spheres entering water vertically. *Journal of Applied Physics*, *19*, 1109–1121. https://doi.org/10.1063/1.1715027

McGehee, J. R., Hathaway, M. E., & Vaughan Jr, V. L. (1959). *Water-landing characteristics of a reentry capsule* (No. NASA-MEMO-5-23-59L).

Mohammadpour, R., Ghani, A. A., & Azamathulla, H. M. (2013). Numerical modeling of 3-D flow on porous broad crested weirs. *Applied Mathematical Modelling*, *37*(22), 9324-9337. https://doi.org/10.1016/j.apm.2013.04.041

Rabbi, R., Speirs, N. B., Kiyama, A., Belden, J. L., & Truscott, T. T. (2020). Impact force reduction by consecutive water entry of spheres. *Journal of Fluid Mechanics*, *915*, A55. https://doi.org/10.1017/jfm.2020.1165

Renda, F., Giorgio-Serchi, F., Boyer, F., & Laschi, C. (2015, May). *Locomotion and elastodynamics model of an underwater shell-like soft robot.* 2015 IEEE International Conference on Robotics and Automation (ICRA) (pp. 1158-1165). IEEE.

Ropert-Coudert, Y., Grémillet, D., Ryan, P., Kato, A., Naito, Y., & Le Maho, Y. (2004). Between air and water: the plunge dive of the Cape Gannet Morus capensis. *Ibis*, *146*(2), 281-290. https://doi.org/10.1111/j.1474-919x.2003.00250.x

Seddon, C. M., & Moatamedi, M. (2006). Review of water entry with applications to aerospace structures. *International Journal of Impact Engineering*, *32*, 1045–1067. https://doi.org/10.1016/j.ijimpeng.2004.09.002

Souli, M., Messahel, R., Cohen, B., & Aquelet, N. (2014). *LS-DYNA Users conference session: fluid structure interaction 1-1 numerical investigation of phase change and cavitation effects in nuclear power plant pipes.* Engineering, Environmental Science, Physics.

Speirs, N. B., Langley, K. R., Pan, Z., Truscott, T. T., & Thoroddsen, S. T. (2021). Cavitation upon low-speed solid–liquid impact. *Nature Communications*, *12*, 7250. https://doi.org/10.1038/s41467-021-27383-5

Tang, B., Xu, J., Jia, Y., & Yu, J. (2017). Short fiber-reinforced EPDM coating film superelastic constitutive model. *Chinese Journal of Mechanics*, *49*(2), 317-323. https://doi.org/10.6052/0459-1879-16-324

Tang, Z., Luo, Q., Leng, X., Liu, P., & Luo, J. (2016). Surge detecting with a spherical sensor. *Sensor Review*, *36*(2), 130-139. https://doi.org/10.1108/SR-12-2014-0765

Techet, A. H., & Truscott, T. T. (2011). Water entry of spinning hydrophobic and hydrophilic spheres. *Journal of Fluids and Structures*, *27*, 716–726. https://doi.org/10.1016/j.jfluidstructs.2011.03.014

Thomas, W. L. (1975). *Ditching investigation of a 1/20-scale model of the space shuttle orbiter* (No. NASA-CR-2593). NASA.

Thompson, W. C., United States., & Langley Research Center. (1965). *Dynamic model investigation of the landing characteristics of a manned spacecraft*. Washington, D.C.: National Aeronautics and Space Administration.

Truscott, T. T., Epps, B. P., & Techet, A. H. (2012). Unsteady forces on spheres during free-surface water entry. *Journal of Fluid Mechanics*, *704*, 173–210. https://doi.org/10.1017/jfm.2012.232

Truscott, T.T., Epps, B. P., & Belden, J. L. (2014). Water entry of projectiles. *Annual Review of Fluid Mechanics*, *46*, 355–378. https://doi.org/10.1146/annurev-fluid-011212-140753

Varas, D., Zaera, R., & López-Puente, J. (2009). Numerical modelling of the hydrodynamic ram phenomenon. *International Journal of Impact Engineering*, *36*, 363–374. https://doi.org/10.1016/j.ijimpeng.2008.07.020

Vaughan, V. L., & United States. (1959). *Water landing impact accelerations for three models of reentry capsules*. Washington, D.C.: National Aeronautics and Space Administration.

Wang, T. M., Yang, X. B., Liang, J. H., Yao, G. C., & Zhao, W. (2013). CFD based investigation on the impact acceleration when a gannet impacts with water during plunge diving. *Bioinspiration & Biomimetics*, 8.036006. https://doi.org/10.1088/1748-3182/8/3/036006

Wehner, M., Truby, R. L., Fitzgerald, D. J., Mosadegh, B., Whitesides, G. M., Lewis, J. A., & Wood, R. J. (2016). An integrated design and fabrication strategy for entirely soft, autonomous robots. *Nature*, *536*(7617), 451-455. https://doi.org/10.1038/nature19100

Wood, R.W. (1909). A study of splashes. *Science*, *29*, 464–465.

https://doi.org/10.1126/science.29.742.464

Xu, L., Troesch, A., & Peterson, R. (1999). Asymmetric hydrodynamic impact and dynamic response of vessels. *Journal of Offshore Mechanics and Arctic Engineering-transactions of The Asme*, *121*, 83–89. https://doi.org/10.1115/1.2830082

Yang, L., Sun, T., Wei, Y., Wang, C., Xia, W., & Wang, Z. (2021a). Hydroelastic analysis of water entry of deformable spheres. *Journal of Hydrodynamics*, *33*, 821–832. https://doi.org/10.1007/s42241-021-0065-1

Yang, L., Wei, Y., Wang, C., Xia, W., & Li, J. (2020a). Numerical investigations on the deformation styles and stress distributions of hyperelastic/viscoelastic spheres during water entry. *Journal of Applied Physics*, *127*(6), 064901. https://doi.org/10.1063/1.5130069

Yang, L., Wei, Y., Wang, C., Xia, W., Li, J., & Chen, C. (2020b). Numerical study on the deformation behaviors of elastic spheres during water entry. *Journal of Fluids and Structures*, *99*, 103167. https://doi.org/10.1016/j.jfluidstructs.2020.103167

Yang, L., Wei, Y., Wang, C., Xia, W., Li, J., Wang, Z., & Zhang, D. (2021b). Dynamics of the cavity evolution during vertical water entry of deformable spheres. *Physics of Fluids*, *33*, 065106. https://doi.org/10.1063/5.0051401

Zhang, L., Wang, Z., & Jia, H. (2023). Effect of wave phases and heights on supercavitation flow field and dynamic characteristics of successively fired high-speed projectiles. *Journal of Marine Science and Engineering*, *11*, 629. (1–17). https://doi.org/10.3390/jmse11030629